TOPICAL COLLECTION: 2021 METALLURGICAL PROCESSES WORKSHOP FOR YOUNG SCHOLARS

Revealing the Viscosity–Structure Relationship of SiO_2–MnO–CaO Fluxes Geared Toward High Heat Input Submerged Arc Welding

CONG WANG, ZHANJUN WANG, and JIAKUN YANG

In this study, the influence of MnO substitution with CaO on the viscosity and structure of ternary SiO_2–MnO–CaO submerged arc welding fluxes was investigated. The results showed that the viscosity increased with the substitution of MnO with CaO, which was correlated to the enhancement in the degree of polymerization of the flux structural units as the activation energy increased from 96.2 to 125.5 kJ/mol for viscous flow. Deconvolution and area integration of the Raman spectra of the fluxes revealed that the Q^3/Q^2 ratio (Q^i, where i is the number of bridging oxygen in one [SiO_4]-tetrahedral unit) increased and NBO/Si (nonbridging oxygen per silicon atom) decreased with higher CaO/(MnO + CaO) mass ratios. It was also observed from the O_{1s} X-ray photoelectron spectroscopy (XPS) that the relative proportion of O^0 and O^{2-} increased at the cost of O^-, indicating the polymerization of the fluxes, which correlated well with the Raman spectra results and the viscous behavior.

https://doi.org/10.1007/s11663-021-02391-4

I. INTRODUCTION

UNDER the surging demand of ultralarge ships, ultralong span bridges, *etc*., low-carbon low-alloy steel grades possessing excellent weldability and satisfactory mechanical properties have been under tremendous investigation.[1–4] Weldability is one of the crucial factors ensuring end-user properties of steel products, where the welding flux is essential to meet the requirements of arc stability, slag detachability, *etc*., particularly under high heat input submerged arc welding processes.[5–7]

A fundamental understanding of the physicochemical properties of the welding flux, especially high-temperature viscosity, constitutes a prerequisite for the design of the welding flux to minimize unnecessary defects and excessive dissolution of unwanted impurities in the weld zone. The viscosity of the welding flux can be correlated to the spreading phenomenon on the weld joint and assist in the arc concentration, and it can affect the crystallization behavior and wettability of the flux, which directly determines the weld formability and slag detachability.[8,9] Moreover, all pertinent physicochemical properties are essentially regulated by the structure of the welding flux. However, only limited studies have been documented regarding the physicochemical properties and corresponding structures of the interested welding flux systems.[2,8,10–12]

Si and Mn are fundamental alloying elements in the low-carbon low-alloy steels, and fine-tuned Si and Mn contents in the weld metal are beneficial for the optimization of ductility and low-temperature impact toughness.[13] For high-Mn steels, Mn in the weld metal can be directly controlled by Mn-containing welding wire; however, for low-carbon low-alloy steels, it is preferable to employ fused SiO_2–MnO-based welding fluxes that can decompose and release O, Si, and Mn elements under the synergy of arc plasma and slag–metal reaction, and eventually promote the transfer of O, Si, and Mn elements to the weld metal.[5,14] In addition, SiO_2, as a network former, has a great influence on the viscosity of the welding flux and can effectively guarantee discrete separation of the metal from the flux and improve the arc stability of the flux,[15,16] and the addition of MnO in the welding flux can improve the metal deposition efficiency of submerged arc welding.[14] It is noteworthy that excessive O can easily lead to deteriorated fracture toughness and ductility of the weld metal.[17,18] Thus, substitution of an appropriate amount of MnO with CaO in SiO_2–MnO-based welding flux to compensate for the reduction of SiO_2 has been suggested.[6,18] Furthermore, a proper amount of CaO can also facilitate dephosphorization and desulfurization, improve arc stability, and increase the impact strength of the weld joint.[16] However, to the authors' best

---

CONG WANG, ZHANJUN WANG, and JIAKUN YANG are with the School of Metallurgy, Northeastern University, Shenyang 110819, China. Contact e-mail: wangc@smm.neu.edu.cn

Manuscript submitted August 30, 2021, accepted November 11, 2021.

knowledge, detailed studies on the physicochemical properties, and, in particular, viscosity–structure relationship of the SiO_2–MnO–CaO flux system, have yet to be fully understood.

In this study, the substitutional effect of MnO with CaO on the viscous behavior of the SiO_2–MnO–CaO flux system at various temperatures was investigated and correlated with the flux structure using Raman spectroscopy and X-ray photoelectron spectroscopy (XPS), which may further the understanding of the crystallization behavior of the welding flux as well as the transfer behavior of alloying elements caused by the slag–metal reaction and offer a viable way to achieve the desired optimal flux design.

II. EXPERIMENTAL

A. *Sample Preparation*

All flux samples were prepared using reagent grade powders of SiO_2 (> 98 wt pct), MnO (> 99 wt pct), and CaO (> 98 wt pct), which were calcinated for 10 hours in advance at 1000 °C in a muffle furnace to remove moisture or other easily decomposable chemical ingredients. The designed chemical compositions of the flux samples are presented in Table I. Approximately 50 g of powder flux samples were thoroughly mixed and placed inside a molybdenum crucible. The flux samples were then premelted in a vertical resistance furnace at 1550 °C for 1 hour to ensure the homogeneity of the melted fluxes. The entire premelting experiment was protected by high-purity Ar gas (> 99.999 pct) at the flow rate of 0.3 L/min. After premelting, the molten fluxes were rapidly quenched by cold water and pulverized for subsequent experiments. The chemical compositions of the quenched fluxes were confirmed by X-ray fluorescence [XRF, ZXS Priums II, Rigaku (Tokyo)], as shown in Table I, which exhibits a negligible difference in the chemical compositions before and after premelting. It should be mentioned that Mn^{2+} cations can be stable in high-temperature molten fluxes.[19,20] Thus, the weighed compositions were used in the subsequent analysis. In addition, the crystalline state of the quenched fluxes was analyzed by X-ray diffraction [XRD, D8 Advance, Bruker (Berlin)] using Cu K_α radiation at a voltage of 40 kV and a current of 30 mA, where the 2-theta scanning range of the XRD experiment was set between 15 and 90 deg at a scanning rate of 2 deg/min and an increment of 0.02 deg.

B. *Viscosity Measurements*

The viscosity of the fluxes was measured using the rotating cylinder method with a Brookfield digital viscometer instrument [DV2T, Brookfield Engineering Laboratories (Middleboro, MA)]. Before measurement, the viscometer was calibrated using a standard silicone oil at room temperature. A molybdenum crucible containing 120 g flux was placed in the uniform temperature zone of the vertical resistance furnace and protected with a graphite crucible. Then, the crucible together with the flux was heated to 1550 °C and kept at this temperature for 30 minutes to obtain a homogeneous molten flux. The viscosity of the flux was initially measured at 1550 °C with a rotor speed of 20 rpm, and then the viscosity was recorded during continuous cooling at a cooling rate of 5 °C/min. After the viscosity measurement under the continuous cooling condition, the flux was reheated to 1500 °C, 1450 °C, and 1400 °C and kept at different temperatures for 30 minutes; then, the viscosity was measured at 1500 °C, 1450 °C, and 1400 °C, respectively. High-purity Ar gas (> 99.999 pct) at the flow rate of 0.3 L/min was also employed during all of the viscosity measurements. Additional details of the viscosity measurements can be found in the previous studies.[21,22]

C. *Structural Analysis*

Raman spectroscopy [HR-800, Horiba (Paris, France)] and XPS [Escalab 250Xi, Thermo Fisher Scientific Inc. (Waltham, MA)] were employed to semiquantitatively analyze the structure of the quenched fluxes. Raman analysis was performed by a laser confocal Raman spectrometer with the excitation wavelength of 532 nm and the shift range of 200 to 2000 cm^{-1}. The recorded Raman spectra curves were deconvoluted using PeakFit software (PeakFit-Jandel Scientific Software (San Rafael, CA)). The relative fractions of different Q^n (n is the number of bridging oxygen (O^0) in one $[SiO_4]$-tetrahedral unit) units were calculated from the area fractions of the optimal-fitted Gaussian curves.[21,23,24] The O_{1s} XPS spectrum was measured using an X-ray photoelectron spectrometer with a monochromatic Al K_α source. The XPS curves were calibrated with the C_{1s} binding energy at 284.8 eV, and the O_{1s} related peaks were fitted by a similar approach to the Raman spectra analysis to determine the fractions of O elements with different linking characteristics [bridging oxygen (O^0), nonbridging oxygen (O^-), and free oxygen (O^{2-})].

III. RESULTS AND DISCUSSION

A. *Crystalline State of the Quenched SiO_2–MnO–CaO Fluxes with Different CaO/(MnO + CaO) Mass Ratios*

XRD analysis was performed on the quenched fluxes, and the results are shown in Figure 1. It can be observed that all XRD patterns uniformly exhibit broad diffusion peaks with amorphous characteristics in the 2θ range of 20 to 40 deg. The amorphous state of the welding fluxes is an extremely influential technical indicator for the manufacturing of the submerged arc welding fluxes, which can reflect the uniformity of the premelted flux composition to facilitate slag detachability, weld formability, and arc stability in the later welding processes. In addition, the amorphous state of the fluxes indicates that the quenched fluxes maintain the state of the fluxes at high temperature and can be used for subsequent structural analysis.

Table I. Pre- and Post-experimental Compositions of the Flux Samples (Weight Percent)

	Pre-experimental Composition (Weighed)				Postexperimental Composition (XRF)			
Sample	SiO_2	MnO	CaO	CaO/(MnO + CaO)	SiO_2	MnO	CaO	CaO/(MnO + CaO)
S1	40	60	0	0	37.98	62.02	0	0
S2	40	50	10	0.17	38.95	51.45	9.60	0.17
S3	40	40	20	0.33	39.56	41.50	18.94	0.34
S4	40	30	30	0.50	40.49	30.80	28.71	0.52
S5	40	20	40	0.67	41.09	20.31	38.60	0.69
S6	40	10	50	0.83	40.98	9.82	49.20	0.84

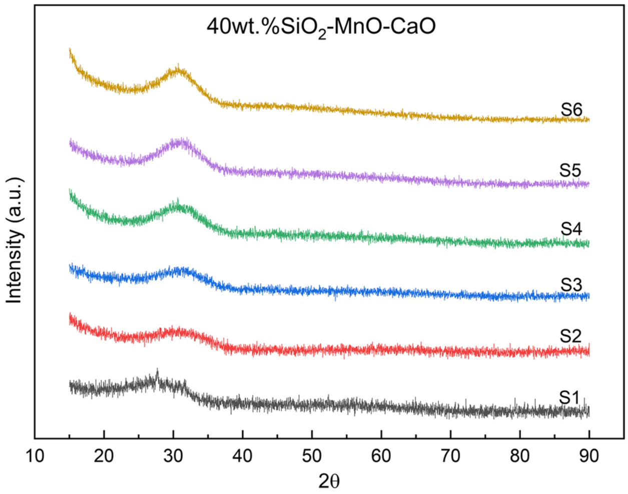

Fig. 1—XRD patterns of the quenched fluxes.

B. *Effect of CaO/(MnO + CaO) Mass Ratio on the Viscosity of SiO_2–MnO–CaO Fluxes*

Figure 2(a) shows the viscosity of SiO_2–MnO–CaO fluxes as a function of CaO/(MnO + CaO) mass ratios at temperatures of 1550, 1500, 1450, 1400. It can be seen that the viscosity shows an increasing trend with the increase of CaO/(MnO + CaO) mass ratios, which is further manifested for fluxes with CaO contents higher than 30 wt pct. In addition, the viscosity of the fluxes in the temperature range of 1550 to 1400 is between 0.1 and 0.6 Pa s, indicating an excellent fluidity of the welding fluxes, which is conducive to the weld formability in the actual welding process. Figure 2(b) exhibits the viscosity of SiO_2–MnO–CaO fluxes at different temperatures. As expected, the viscosity in the Newtonian fluid region increases steadily as the temperature decreases. For fluxes with CaO contents of 0, 10, and 40 wt pct, a sharp increase in the viscosity was observed at a certain temperature, which can be identified as the "break temperature."[25] It is usually inaccessible to directly explore what happens at the break temperature of the fluxes due to the continuous process of the viscosity measurement. The recognized prerequisite for the occurrence of break temperature is that considerable crystals must be present at the breakpoint to have an abrupt increase in the viscosity value.[10,25] However, considering the behavior of long and short slag in steelmaking slags,[26] break temperature may also be related to the crystallization rate of the primary phase.

In order to further explore the relationship between the break temperature and the primary phase, FactSage 8.0 software was employed to estimate the phase crystallization fraction of the fluxes at various temperatures, as shown in Figure 3. It can be seen that with the increase of the CaO content, the primary phase of the fluxes changed from $MnSiO_3$ to $CaSiO_3$, and then to Ca_2SiO_4 (Mn_2SiO_4), and the crystallization rates of the primary phase of the fluxes with CaO contents of 0, 10, and 40 wt pct were significantly higher than those of the fluxes with CaO contents of 20, 30, and 50 wt pct, resulting in a discernible break temperature in the viscosity curves (Figure 2) for the fluxes with CaO contents of 0, 10, and 40 wt pct. Thus, it can be inferred that when the temperature drops to the crystallization temperature, the break temperature can be determined for the flux with a considerable rapid crystallization rate. Otherwise, the break temperature may not be detected for the flux with a comparable flat crystallization rate; *i.e.*, the break temperature does not necessarily appear when a certain number of crystals have accumulated in the molten flux.

The relationship between viscosity and temperature can be expressed by the Arrhenius formula:[21]

$$\eta = \eta_0 \exp(E_a/RT) \quad [1]$$

where η (Pa s) is the viscosity value, η_0 represents the viscosity constant, E_a (kJ/mol) refers to the activation energy of viscous flow, R (J mol^{-1} K^{-1}) is the universal gas constant, and T (K) is the absolute temperature. In a silicate flux melt, the activation energy of viscous flow indicates the resistance caused by electrostatic force that needs to be overcome between different ions and ion clusters in the melt.[27] In the present study, the viscous activation energy of fluxes with

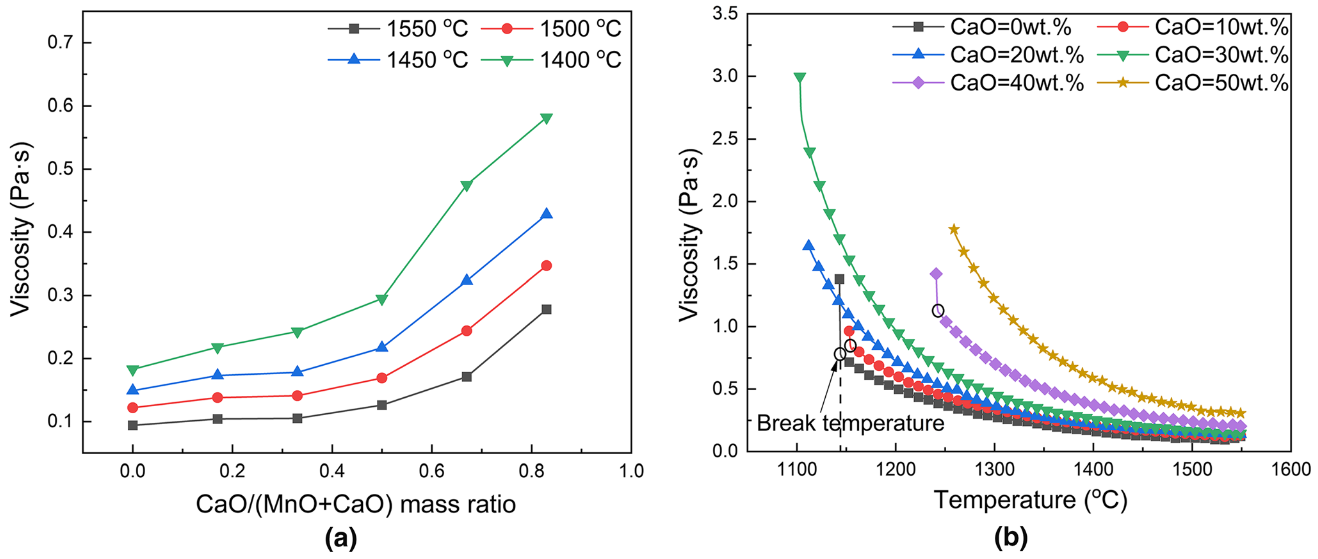

Fig. 2—(*a*) Viscosity of SiO_2–MnO–CaO fluxes as a function of CaO/(MnO + CaO) mass ratios. (*b*) Viscosity of SiO_2–MnO–CaO fluxes at different temperatures.

different CaO/(MnO + CaO) mass ratios can be calculated from the slope of the fitted line between the natural logarithm of viscosity (ln η) *vs* reciprocal temperature ($1/T$) in the Newtonian fluid region, as shown in Figure 4. As can be seen, the activation energy gradually increases from 96.19 to 125.52 kJ/mol with CaO/(MnO + CaO) mass ratio increases from 0 to 0.84, indicating that the viscous resistance is increased, which is consistent with the increased viscosity shown in Figure 2. The changes in viscosity and viscous activation energy are essentially related to the melt structure. Thus, it can be speculated that the increased CaO/(MnO + CaO) mass ratio may lead to the polymerization of the flux structure and the expanded size of silicon ion clusters, which needs to be further verified by subsequent structural analysis.

C. *Effect of CaO/(MnO + CaO) Mass Ratio on the Structure of SiO_2–MnO–CaO Fluxes*

The Raman spectra curves of the fluxes in the shift range of 500 to 1300 cm^{-1} are shown in Figure 5(a). The characteristic peaks located in the region of 600 to 800 cm^{-1} mainly correspond to the bending vibration of Si–O–Si between different $[SiO_4]$-tetrahedral units.[12,28,29] For the characteristic peaks located in the region of 800 to 1200 cm^{-1}, the Raman spectra in 840 to 870 cm^{-1}, 900 to 930 cm^{-1}, 950 to 980 cm^{-1}, and 1030 to 1060 cm^{-1} can be attributed to the stretching vibration of Si-O^- in Q^0 ($[SiO_4]^{4-}$, monomer), Q^1 ($[Si_2O_7]^{6-}$, dimer), Q^2 ($[SiO_3]^{4-}$, chain or ring), and Q^3 ($[Si_2O_5]^{2-}$, sheet) in the $[SiO_4]$-tetrahedral units based structure, respectively.[30–35] As the CaO/(MnO + CaO) mass ratio increases, the aforementioned characteristic peaks shift to the higher shift, indicating the polymerization behavior of the entire silicate structure. The characteristic peak of individual $[SiO_4]$-tetrahedral units can be determined by performing Gaussian fitting on the Raman spectra located between 800 and 1200 cm^{-1}, and the area fraction of each $[SiO_4]$-tetrahedral unit can be applied to semiquantitatively characterize the content variation of the corresponding structural unit. The typical deconvolution result of the Raman spectra curve of the SiO_2–MnO–CaO flux is shown in Figure 5(b) (detailed fitted results of XPS spectra for all the samples can be found in the Supplemental Material). As can be seen from the semiquantitative area fraction changes of the corresponding structural units shown in Figure 5(c), the fluxes are dominated by Q^2 structural units, accompanied by the relatively low content of Q^0, Q^1, and Q^3 structural units. The reaction between different Q^n units can be described by Eqs. [2] and [3].[36] With the increase of the CaO/(MnO + CaO) mass ratio, the fractions of the Q^0 and Q^2 structural units gradually decrease and the fractions of the Q^1 and Q^3 structural units increase, indicating that simple monomer and chain/ring structural units gradually polymerize into complex dimer and sheet structural units.

$$2Q^1 \leftrightarrow Q^0 + Q^2 \qquad [2]$$

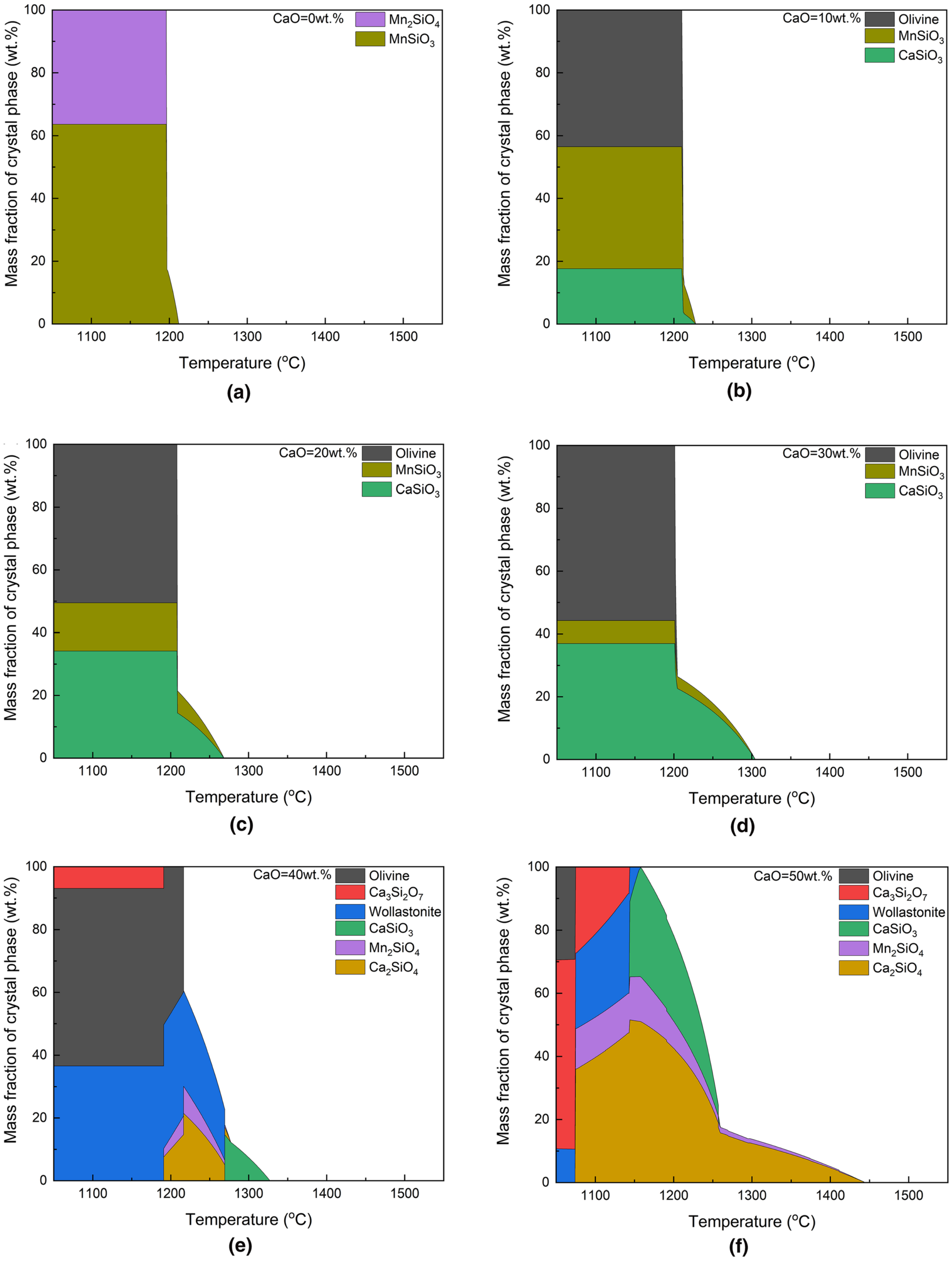

Fig. 3—Calculated results of the mass fraction of different crystal phases precipitated in SiO_2–MnO–CaO fluxes with different CaO contents: (*a*) CaO = 0 wt pct, (*b*) CaO = 10 wt pct, (*c*) CaO = 20 wt pct, (*d*) CaO = 30 wt pct, (*e*) CaO = 40 wt pct, and (*f*) CaO = 50 wt pct.

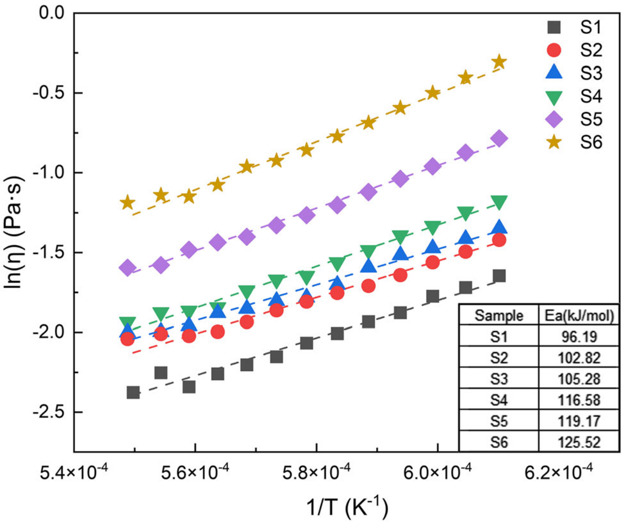

Fig. 4—Natural logarithm of viscosity (ln *η*) *vs* reciprocal temperature (1/*T*) in the Newtonian fluid region. Dotted lines represent the linear fitting of the data.

$$2Q^2 \leftrightarrow Q^1 + Q^3 \qquad [3]$$

For the fluxes with fixed SiO_2 content, it can be seen that the equal mass substitution between CaO and MnO with the same cation valence will lead to a certain degree of fluctuation on the melt structure. Among the various parameters that link the structure of the fluxes with physicochemical properties, NBO/Si (nonbridging oxygen per silicon atom) and the Q^3/Q^2 area fraction ratio are the most representative indices to characterize the degree of polymerization of the flux structure, where the degree of polymerization in the silicate network is proportional to the Q^3/Q^2 area fraction ratio and is inversely proportional to that of NBO/Si.[37,38] The variations of NBO/Si and the Q^3/Q^2 area fraction ratio as a function of the CaO/(MnO + CaO) mass ratio are shown in Figure 5(d). It can be seen that with the increase of the CaO/(MnO + CaO) mass ratio, the NBO/Si decreases and the Q^3/Q^2 area fraction ratio increases, indicating an enhancement in the degree of polymerization of the flux structure.

Generally, MnO and CaO can decompose free oxygen ions (O^{2-}) to depolymerize the complex network structure into the simple network structure. It can be seen that the network depolymerization capability of MnO is greater than that of CaO, which is consistent with the results observed by Zhang and Chou.[39] According to McMillan[40] and Park,[41] the depolymerization capability of different metal oxides can be attributed to the difference in the strength of the M-O bonds, and the doubly charged cations (M^{2+}) with large ionic radius and small ionization potential (Z/r^2) should preferentially occupy the more coupled Q^3 sites, while the smaller M^{2+} cations with larger ionization potential and smaller ionic radius will favor the higher charged concentration offered by the Q^2 sites. Mn^{2+} and Ca^{2+} cations coexist in the form of $[MnO_6]$-octahedral and $[CaO_6]$-octahedral units in the silicate structure, respectively.[42] Since the ionization potential of Ca^{2+} is lower than that of Mn^{2+} $\left(Z = 2, R_{Ca^{2+}} > R_{Mn^{2+}}, Z\big/R^2_{Ca^{2+}} < Z\big/R^2_{Mn^{2+}}\right)$ and the cage size of the $[CaO_6]$-octahedral unit is larger than that of the $[MnO_6]$-octahedral unit, the Ca^{2+} cation maintains a charge balance with the nonbridging oxygens linked to two different silicon atoms, while the Mn^{2+} cation maintains a charge balance with the nonbridging oxygens shared by two adjacent corners on the same silicon atom.[38] Thus, the substitution of MnO with CaO reduces NBO/Si and increases the Q^3/Q^2 area fraction ratio, thereby enhancing the degree of polymerization of the flux structure.

To further clarify the effect of CaO/(MnO + CaO) mass ratios on the structure of the SiO_2–MnO–CaO fluxes, the semiquantitative XPS technique was employed to analyze the structural transformation caused by the changes in the relative amount of tetrahedrons under various coordination conditions. The binding energies around 532, 531, and 530 eV can be assigned to the vibration of bridging oxygen (O^0), nonbridging oxygen (O^-), and free oxygen (O^{2-}) ions, respectively.[43,44] A schematic diagram of the deconvolution results of the typical O_{1s} XPS peak is shown in Figure 6(a) (detailed fitted results of XPS spectra for all the samples can be found in the Supplemental Material), where the mole fraction of different oxygen ions can be determined by integrating the areas under the deconvoluted peaks. Figure 6(b) depicts the changes in the mole percent of O^{2-}, O^-, and O^0 as a function of CaO/(MnO + CaO) mass ratios. As can be seen from Figure 6(b), the mole percent of O^- decreases and that of O^0 increases with higher CaO/(MnO + CaO) mass ratios, indicating an increasing trend of degree of polymerization that leads to a higher viscosity, which is consistent with the variation trend of the semiquantitative Raman analysis. The equilibrium reaction of different types of oxygen ions coexisting in the molten fluxes can be described by Eqs. [4] and [5], where O^{2-} can react with O^0 to form O^- to break the existing bonds, thereby depolymerizing the melt structure and decreasing the viscosity.

$$O^0 + O^{2-} = 2O^- \qquad [4]$$

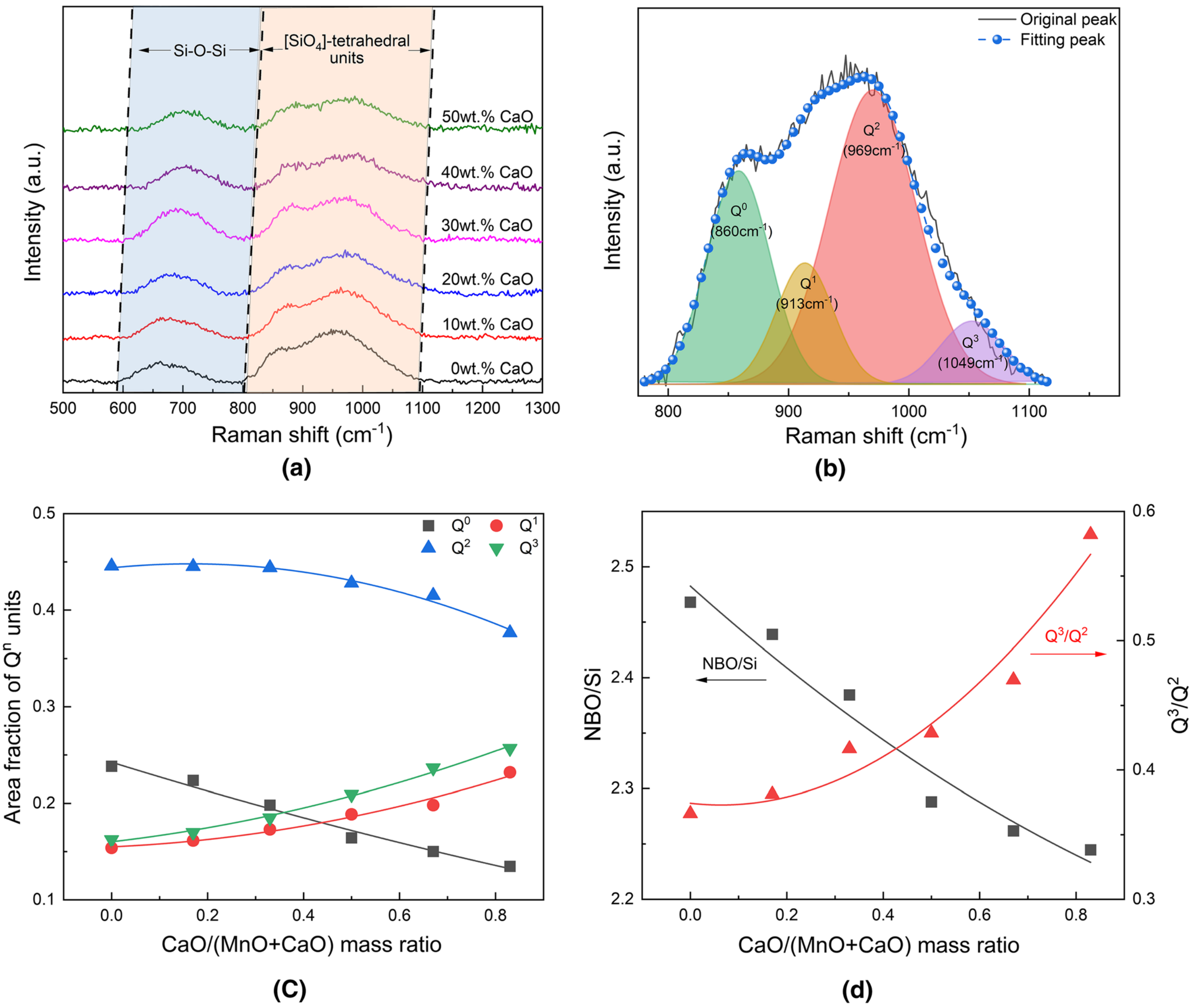

(a)

(b)

(C)

(d)

Fig. 5—(*a*) Original Raman spectra curves of the fluxes. (*b*) Typical deconvoluted results of the Raman spectra. (*c*) Changes in the area fraction of Q^n units with different CaO/(MnO + CaO) mass ratios. (*d*) Variation of NBO/Si and Q^3/Q^2 fraction ratio with different CaO/(MnO + CaO) mass ratios.

$$\mathrm{Si{-}O{-}Si} + \mathrm{O}^{2-} = 2\mathrm{Si} - \mathrm{O}^{-} \qquad [5]$$

Essentially, as the mixture of different oxides melts at high temperatures, the electrons in the system will be rearranged and transported in the melt structure with oxygen ions as carriers. The influence of the substitution between MnO and CaO on the silicate melt network structure can be achieved by disrupting the connection between Si and O^0 in the Si–O–Si linkages. Mn^{2+} cations with a smaller ion radius and a larger ionization potential are conducive to the formation of Q^2 units and promote the process of Eq. [3].[41] Under such circumstances, with the continuous increase of CaO/(MnO + CaO) mass ratio, the contents of O^0 and O^{2-} gradually increase, which offsets the fraction of O^-, thereby causing a series of changes in the structure of the fluxes. In other words, the emergence of new bridging oxygen indicates the transformation of simple structural units into complex structural units, thereby causing significant changes in different species of structural units, which has also been verified in Raman spectroscopy analysis.

IV. CONCLUSIONS

In this study, the viscosity-structure correlations of SiO_2–MnO–CaO welding fluxes are systematically analyzed by the rotating cylinder method coupled with Raman and XPS techniques, and the following conclusions are drawn.

1. The viscosity and apparent activation energy both increase upon the substitution of MnO with CaO,

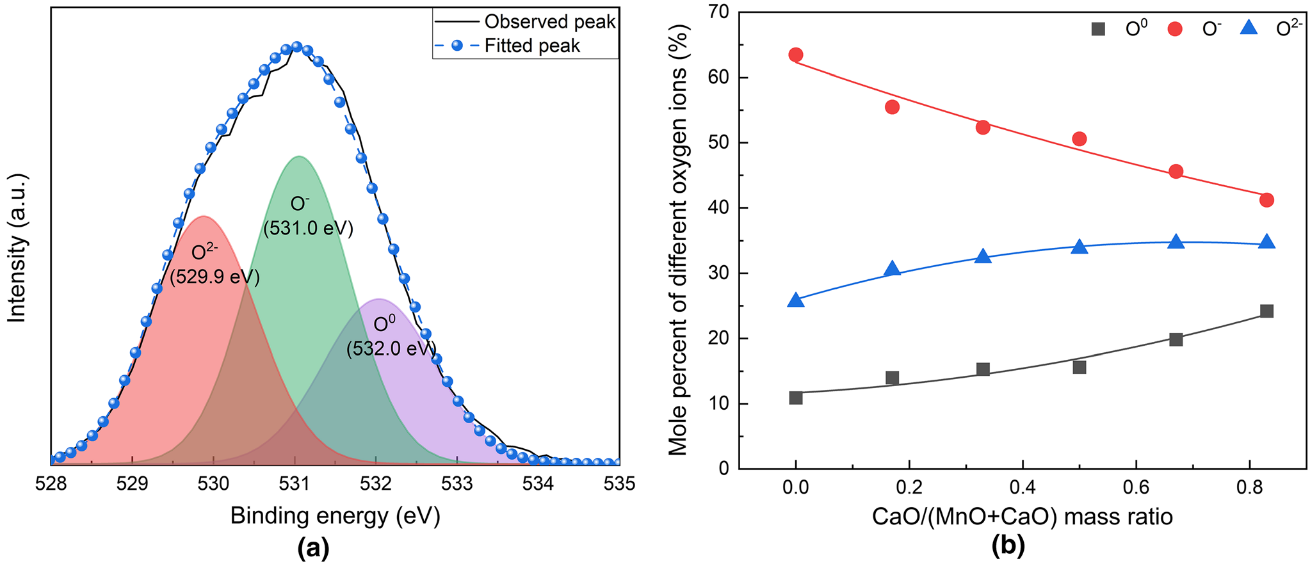

Fig. 6—(*a*) Typical deconvolution result of O_{1s} bending energy in the XPS curve. (*b*) Mole fraction of different oxygen ions.

indicating the formation of more complex structural units.

2. The Q^3/Q^2 ratio increases and the NBO/Si value decreases with the substitution of MnO with CaO, indicating a higher degree of polymerization in the silicate network structure.
3. The substitution of MnO with CaO can decrease the fraction of nonbridging oxygen and enhance the fraction of bridging oxygen in the fluxes, indicating MnO has a stronger depolymerization capability than that of CaO.

ACKNOWLEDGMENTS

The authors sincerely thank the National Natural Science Foundation of China (Grant Nos. 52104295, U20A20277, 51861145312, 52050410341, and 52011530180), Royal Academy of Engineering (Grant No. TSPC1070), and Research Fund for Central Universities (Grant No. N2025025). This work is also funded by the Regional Innovation Joint Fund of Liaoning Province (Grant No. 2020-YKLH-39).

CONFLICT OF INTEREST

On behalf of all authors, the corresponding author states that there is no conflict of interest.

SUPPLEMENTARY INFORMATION

The online version contains supplementary material available at https://doi.org/10.1007/s11663-021-02391-4.

REFERENCES

1. Z. Wang, G. Wen, Q. Liu, P. Tang, W. Jiang, and S. Huang: *Metall. Mater. Trans. B*, 2021, vol. 52B, pp. 1574–81.
2. J.B. Kim and I. Sohn: *ISIJ Int.*, 2014, vol. 54, pp. 2050–58.
3. X. Zou, L. Zhou, H. Matsuura, and C. Wang: *JOM*, 2021, vol. 73, pp. 1110–17.
4. X. Wu, S. Wu, C. Yan, X. Ma, and Q. Zhang: *Metall. Mater. Trans. B*, 2021, vol. 52B, pp. 1012–22.
5. J. Zhang, C. Wang, and T. Coetsee: *Metall. Mater. Trans. B*, 2021, vol. 52B, pp. 1937–44.
6. J. Zhang, T. Coetsee, H. Dong, and C. Wang: *Metall. Mater. Trans. B*, 2020, vol. 51B, pp. 1953–57.
7. J.E. Indacochea, M. Blander, N. Christensen, and D.L. Olson: *Metall. Mater. Trans. B*, 1985, vol. 16B, pp. 237–45.
8. J.B. Kim, J.K. Choi, I.W. Han, and I. Sohn: *J. Non-Cryst. Solid*, 2016, vol. 432, pp. 218–26.
9. Z. Duan, R. Qin, and H. Guo: *Metall. Mater. Trans. A*, 2014, vol. 45A, pp. 843–53.
10. J.B. Kim and I. Sohn: *J. Non-Cryst. Solid*, 2013, vol. 379, pp. 235–43.
11. J.B. Kim and I. Sohn: *ISIJ Int.*, 2014, vol. 54, pp. 657–63.
12. Y. Zhang, T. Coetsee, H. Yang, T. Zhao, and C. Wang: *Metall. Mater. Trans. B*, 2020, vol. 51B, pp. 1947–52.
13. C. Wang and J. Zhang: *Acta Metall. Sinica*, 2021, vol. 57, pp. 1126–40.
14. A. Cruz-Crespo, R.Q. Puchol, L. González, C. Pérez, E.D. Cedré, and J.G. Jacomino: *Weld. Int.*, 2010, vol. 24, pp. 518–23.
15. J. Zhang, T. Coetsee, and C. Wang: *Metall. Mater. Trans. B*, 2019, vol. 51B, pp. 16–21.
16. B. Ferrera and D.L. Olson: *Weld. J.*, 1975, vol. 54, pp. 211–15.
17. J. Jang and J.E. Indacochea: *J. Mater. Sci.*, 1987, vol. 22, pp. 689–700.
18. B. Chai and T.W. Ea Car: *Weld. J.*, 1982, vol. 61, pp. 229–32.
19. Y. Zou, H. Gu, and A. Huang: *J. Am. Ceram. Soc.*, 2018, vol. 101, pp. 2096–06.
20. Y. Fujii, Y. Nakai, Y.I. Uchida, and Y. Miki: *ISIJ Int.*, 2017, vol. 101, pp. 524–29.
21. Z. Wang and I. Sohn: *J. Am. Ceram. Soc.*, 2018, vol. 101, pp. 4285–96.
22. Z. Wang, Y. Sun, S. Sridhar, M. Zhang, and Z. Zhang: *Metall. Mater. Trans. B*, 2017, vol. 48B, pp. 527–37.
23. X. Yan, W. Pan, X. Wang, X. Zhang, and Q. Wang: *Metall. Mater. Trans. B*, 2021, vol. 52B, pp. 2526–35.

24. J. Yang, L. Wang, Q. Wang, J. Zhang, Y. Sasaki, C. Zhang, D. Cai, and O. Ostrovski: *Steel Res. Int.*, 2021, https://doi.org/10.1002/srin.202100123.
25. S. Sridhar, K.C. Mills, O.D.C. Afrange, H.P. Lorz, and R. Carli: *Ironmak. Steelmak.*, 2000, vol. 27, pp. 238–42.
26. S. Chu, H. Liu, S. Diao, and T. Xu: *Int. J. Min. Met. Mater.*, 1995, vol. 2, pp. 19–23.
27. S. Seetharaman, S. Du, S. Sridhar, and K.C. Mills: *Metall. Mater. Trans. B*, 2000, vol. 31B, pp. 111–19.
28. Y. Chen, F. Lai, and J. Li: *JOM*, 2020, vol. 72, pp. 1414–21.
29. J. Yang, Y. Kim, and I. Sohn: *J. Mater. Res. Technol.*, 2021, vol. 10, pp. 268–81.
30. D. Virgo, B.O. Mysen, and I. Kushiro: *Science*, 1980, vol. 208, pp. 1371–73.
31. Z. Wang, Y. Sun, S. Sridhar, M. Zhang, M. Guo, and Z. Zhang: *Metall. Mater. Trans. B*, 2015, vol. 46B, pp. 537–41.
32. Z. Wang and I. Sohn: *Ceram. Int.*, 2019, vol. 46, pp. 903–12.
33. Y.C. Jeong, S.H. Shin, J.Y. Baek, and J.W. Cho: *Metall. Mater. Trans. B*, 2021, vol. 52B, pp. 2048–55.
34. X. He, L. Wang, and K. Chou: *J. Alloy Compd.*, 2021, vol. 876, p. 160209.
35. E. Gao, W. Wang, and L. Zhang: *J. Non-Cryst. Solids*, 2017, vol. 473, pp. 79–86.
36. J.S. Choi, T.J. Park, D.J. Min, and I. Sohn: *J. Mater. Res. Technol.*, 2021, vol. 15, pp. 1382–94.
37. T. Li, C. Zhao, C. Sun, S. Song, and Q. Wang: *Metall. Mater. Trans. B*, 2020, vol. 51B, pp. 2724–34.
38. J.H. Park: *ISIJ Int.*, 2012, vol. 52, pp. 1627–36.
39. G.H. Zhang and K.C. Chou: *Steel Res. Int.*, 2013, vol. 84, pp. 631–37.
40. P. McMillan: *Am. Mineral.*, 1984, vol. 69, pp. 645–659.
41. J.H. Park: *J. Non-Cryst. Solid*, 2012, vol. 358, pp. 3096–02.
42. H. Chen, Y. Bai, L. Zheng, L. Wu, and J. Xu: *J. Mater. Chem. C*, 2020, vol. 8, pp. 6587–94.
43. H. Kim and I. Sohn: *ISIJ Int.*, 2011, vol. 51, pp. 1–8.
44. W. Liu, Y. Chen, J. Wang, and H. Zuo: *J. Sustain. Metall.*, 2021, vol. 7, pp. 1169–77.